

Probing the Spin Pumping Mechanism: Exchange Coupling with Exponential Decay in $\text{Y}_3\text{Fe}_5\text{O}_{12}$ /barrier/Pt Heterostructures

C. H. Du^{1,†}, H. L. Wang^{1,†}, Y. Pu¹, T. L. Meyer², P. M. Woodward², F. Y. Yang^{1,*}, and P. C. Hammel^{1,*}

¹Department of Physics, The Ohio State University, Columbus, OH, 43210, USA

²Department of Chemistry and Biochemistry, The Ohio State University, Columbus, OH, 43210, USA

[†]These authors made equal contributions to this work

*Emails: fyyang@physics.osu.edu; hammel@physics.osu.edu

Ferromagnetic resonance (FMR) driven spin pumping of pure spin currents from a ferromagnet (FM) into a nonmagnetic material (NM) promises new spin-functional devices with low energy consumption [1-6]. The mechanism of spin pumping is under intense investigation and it is widely believed that exchange interaction between the FM and NM is responsible for this phenomenon [2-5, 7]. We observe a thousand-fold exponential decay of the spin pumping from 20-nm thick $\text{Y}_3\text{Fe}_5\text{O}_{12}$ (YIG) films to platinum across insulating barriers, from which the exponential decay lengths of 0.16 and 0.23 nm are extracted for oxide barriers with band gaps of 4.93 eV and 2.36 eV, respectively. This prototypical signature of quantum tunneling through a barrier underscores the importance of exchange coupling for spin pumping and reveals its dependence on the characteristics of the barrier material.

Generation and manipulation of spin currents is key to spintronic applications [1]. FMR driven spin pumping has been demonstrated to inject a pure spin current through angular

momentum transfer from an FM to an adjacent NM [2-6]. General belief assumes a dynamic coupling via exchange interaction between the precessing magnetization (\mathbf{M}) of the FM and the conduction electrons of the NM at the NM/FM interface. This mechanism will lead to a short, atomic-scale coupling that decays exponentially with separation between the FM and NM. However, this has not been experimentally confirmed, partially due to the large dynamic range needed to measure such rapidly decaying spin pumping signal [6, 8]. Our recent demonstration of large spin pumping in Pt/YIG bilayers with mV-level inverse spin Hall effect (ISHE) voltage, V_{ISHE} , offers a material platform with signal-to-noise ratio sufficient to quantitatively characterize the coupling range, enabling detailed insights into the spin pumping mechanism. We use three different barrier materials, including two oxide insulators and Si, to systematically investigate the barrier thickness t dependence of spin pumping in Pt/barrier(t)/YIG heterostructures. The clear exponential decays of ISHE voltage with characteristic lengths of ~ 0.2 nm for the oxide barriers provide decisive evidence for the predicted exchange coupling model for spin pumping.

Our experiments utilize YIG thin films grown on (111)-oriented $\text{Gd}_3\text{Ga}_5\text{O}_{12}$ (GGG) substrates by an off-axis sputtering technique we developed for epitaxial film growth of complex materials [9-12]. Figure 1a shows a high resolution x-ray diffraction (XRD) scan of a 20-nm YIG film near the YIG (444) peak with clear Laue oscillations, indicating high uniformity throughout the film. The XRD rocking curve in the inset to Fig. 1a gives a full width at half maximum (FWHM) of 0.0185° , demonstrating excellent crystalline quality. Figure 1b shows a representative FMR derivative spectrum for a 20 nm YIG film taken at radio-frequency (rf) $f = 9.65$ GHz and microwave power $P_{\text{rf}} = 0.2$ mW with an in-plane magnetic field, from which the peak-to-peak linewidth (ΔH) of 10 Oe is obtained [13].

Spin pumping measurements are conducted at room temperature using a 5-nm thick Pt layer on 20-nm YIG films, as illustrated in Fig. 1c. The samples with a width of ~ 1 mm and a length of ~ 5 mm are placed in the center of an FMR cavity and a DC magnetic field (\mathbf{H}) is applied in the xz -plane. At resonance, the precessing magnetization transfers angular momentum from YIG to the conduction electrons in Pt by means of dynamical coupling [6, 14], generating a pure spin current, \mathbf{J}_s , in Pt along the z -axis with polarization ($\boldsymbol{\sigma}$) parallel to the YIG magnetization. In the Pt layer, \mathbf{J}_s is converted into a net charge current, $\mathbf{J}_c \propto \mathbf{J}_s \times \boldsymbol{\sigma}$, via inverse spin Hall effect [15-18], resulting in an ISHE voltage along the y -axis. Figure 1d shows the V_{ISHE} vs. H spectra of a Pt/YIG bilayer at $\theta_H = 90^\circ$ and 270° (field in plane) at $P_{\text{rf}} = 200$ mW. The peak value of $V_{\text{ISHE}} = 1.0$ mV is generated at the FMR resonant condition given by the FMR derivative spectrum in Fig. 1e. As \mathbf{H} is reversed from $\theta_H = 90^\circ$ to 270° , V_{ISHE} changes sign and maintains the same magnitude as expected since $\boldsymbol{\sigma}$ changes sign with reversal of \mathbf{M} ($\mathbf{M} \parallel \mathbf{H}$ since H exceeds $4\pi M_s$ at resonance), resulting in a reversed sign of the V_{ISHE} .

Figure 1f shows the angular dependence of normalized $V_{\text{ISHE}}(\theta_H)$ for the Pt/YIG bilayer, which agrees with the green curve of a simple $\sin\theta_H$, confirming that the observed voltage signal comes from FMR spin pumping due to,

$$V_{\text{ISHE}} \propto \mathbf{J}_s \times \boldsymbol{\sigma} \propto \mathbf{J}_s \times \mathbf{M} \propto \mathbf{J}_s \times \mathbf{H} \propto \sin\theta_H. \quad (1)$$

The ISHE voltage of the Pt/YIG bilayer at $\theta_H = 90^\circ$ in Fig. 1g is proportional to power P_{rf} for 0.2 mW $< P_{\text{rf}} < 200$ mW, indicating that the observed mV-level V_{ISHE} is still in the linear regime.

To characterize the coupling range of spin pumping, we insert three different thin, insulating barriers, $\text{Sr}_2\text{GaTaO}_6$ (SGTO) with a band gap $E_g = 4.93$ eV, $\text{Sr}_2\text{CrNbO}_6$ (SCNO) with $E_g = 2.36$ eV and amorphous Si between Pt and YIG as illustrated in Fig. 1c (see Supplementary Information for detailed characteristics of double perovskite $\text{Sr}_2\text{GaTaO}_6$ and $\text{Sr}_2\text{CrNbO}_6$).

Figures 2a-2f show the spin pumping and FMR derivative absorption spectra of Pt/barrier/YIG structures with 0.5-nm $\text{Sr}_2\text{GaTaO}_6$, $\text{Sr}_2\text{CrNbO}_6$ and Si barriers, which reduce the ISHE voltage to 20, 100 and 440 μV , respectively. This sensitivity of the decay rate of V_{ISHE} will be discussed later.

Figures 2g-2i show the angular dependence of normalized V_{ISHE} for Pt/barrier(0.5nm)YIG with the three barriers. The sinusoidal angular dependence is characteristic of ISHE [see Eq. (1)], confirming that the observed signals are due to spin pumping, not artifacts due to thermoelectric or magnetoelectric effects such as anisotropic magnetoresistance (AMR) [19, 20]. Figures 2j-2l show the rf power dependence of V_{ISHE} from $P_{\text{rf}} = 0.2$ mW to 200 mW with an in-plane field ($\theta_{\text{H}} = 90^\circ$) for the three samples, all showing linear relationship between P_{rf} and V_{ISHE} [21].

To understand the systematic behavior of spin pumping across a thin insulating barrier, we plot the dependence of V_{ISHE} (normalized by the Pt/YIG samples with direct contact) on the barrier thickness in Figs. 3a-3c for Pt/ $\text{Sr}_2\text{GaTaO}_6(t)$ /YIG, Pt/ $\text{Sr}_2\text{CrNbO}_6(t)$ /YIG and Pt/Si(t)/YIG heterostructures. Four representative V_{ISHE} vs. H spectra for various barrier thicknesses are shown in Figs. 3e-3f for each series. The mV scale of the Pt/YIG ISHE voltage allows us to observe dramatic, thousand-fold changes in V_{ISHE} . As the barrier thickness increases, V_{ISHE} exhibits a clear exponential decay for all three barrier materials and eventually falls below the noise level at $t = 2$ nm for $\text{Sr}_2\text{GaTaO}_6$ and $\text{Sr}_2\text{CrNbO}_6$ barriers and at $t = 5$ nm for Si barrier. From a least-squares linear fit shown in the semi-log plots in Figs. 3a-3c, we obtain an exponential decay length, $\lambda = 0.16, 0.23$ and 0.74 nm for $\text{Sr}_2\text{GaTaO}_6$, $\text{Sr}_2\text{CrNbO}_6$ and Si barriers, respectively, following,

$$V_{\text{ISHE}} = V_{\text{ISHE}}(t = 0)e^{-t/\lambda}. \quad (2)$$

Given $V_{\text{ISHE}} \propto J_s$, the exponential decay of V_{ISHE} indicates that the pure spin current generated in Pt also decreases exponentially with t , a signature behavior of exchange coupling between FM and NM separated by an insulating barrier. This result is the first direct quantitative evidence of the exchange coupling model for spin pumping.

The exponential dependence of spin pumping on barrier thicknesses can be explained by a process in which the wavefunction of the conduction electrons in Pt tunnels through the barrier, couples with the precessing magnetization of YIG through exchange interaction, and acquires spin polarization via spin-dependent scattering at the barrier/YIG interface [2-5]. At a NM/FM interface, a spin current can be generated either by transmission of spin-polarized electrons from the FM into NM, or by spin-dependent scattering of the conduction electrons in NM at the interface. Given that YIG is an insulator, it is unlikely that spin-polarized electrons flow from YIG into Pt. Consequently, the dominant mechanism is the spin-dependent scattering of conduction electrons in Pt at the Pt/YIG interface via exchange interaction with the precessing magnetization of YIG. When the Pt and YIG are separated by a thin barrier within a tunneling distance, the wavefunction of the conduction electrons in Pt can tunnel through the barrier and couple with YIG, and the tunneling probability depends sensitively on the barrier height.

At the interface between a metal and an insulator or a semiconductor, the relevant barrier is typically the Schottky barrier, Φ_B , which depends on the work function of the metal and the electron affinity, charge carrier type and concentration of the insulator/semiconductor. Schottky barrier heights for Pt/Sr₂GaTaO₆ and Pt/Sr₂CrNbO₆ are not known; here we estimate the values of Φ_B for Pt/Sr₂GaTaO₆ and Pt/Sr₂CrNbO₆ based on published results on metal/perovskite Schottky junctions and correlate them to the extracted decay lengths. It was reported that in Au/SrTiO₃ (Nd-doped, carrier density $10^{17} - 10^{18} \text{ cm}^{-3}$) Schottky junctions [22], the Schottky

barrier height is in the range of 1.4 – 1.7 eV, about half of the SrTiO₃ band gap. At lower carrier concentration, Φ_B is expected to remain in this range [22]. Since Au and Pt have similar work functions (5.47 eV for Au and 5.64 eV for Pt) and both Sr₂GaTaO₆ and Sr₂CrNbO₆ are Sr-based perovskites [23], it is reasonable to expect Φ_B in Pt/Sr₂GaTaO₆ and Pt/Sr₂CrNbO₆ to be half of their barrier band gaps as well. Using band gaps of 4.93 eV (Sr₂GaTaO₆) and 2.36 eV (Sr₂CrNbO₆) determined by optical absorption (see Supplementary Information for details), we estimate $\Phi_B = 2.5$ and 1.2 eV for Pt/Sr₂GaTaO₆ and Pt/Sr₂CrNbO₆, respectively.

For a finite rectangular potential barrier, as illustrated in Figs. 4a and 4b for Sr₂GaTaO₆ and Sr₂CrNbO₆ barriers, respectively, the tunneling transmission coefficient D of electrons is determined by the barrier height Φ_B and width t [24]:

$$D \propto \exp\left[-\frac{2t}{\hbar}\sqrt{2m\Phi_B}\right], \quad (3)$$

where m is the effective mass and \hbar is Planck's constant. Since $V_{\text{ISHE}} \propto J_s \propto D$, Eqs. (2) and (3) imply $1/\lambda \propto \sqrt{\Phi_B}$, as shown in Fig. 4c for Pt/Sr₂GaTaO₆(t)/YIG and Pt/Sr₂CrNbO₆(t)/YIG. The two data points align with the origin, providing further evidence for the exchange coupling model in spin pumping and the role of barrier materials in quantum tunneling.

For Si barriers, the decay length of 0.74 nm is much larger than the 0.16 and 0.23 nm for samples with oxide barriers. Si has a smaller band gap (1.1 eV) than the two oxide barriers, thus we expect a larger decay length. If we use $\Phi_B = 0.55$ eV for Pt on amorphous Si, we estimate a decay length of 0.34 nm using the same rectangular potential barrier model, smaller than observed, indicating a barrier height smaller than half of the Si band gap as we assumed for the oxide barriers. This is not unexpected, however, since the Schottky barrier heights of metal/Si junctions are sensitive to the doping type and carrier concentration. In addition to the mechanism

already discussed, we should also consider the possibility that there may be carriers in the Si barrier allowing either an indirect exchange process or spin diffusion through the barrier [25]. Further investigation of the characteristics of the barriers in spin pumping is needed to obtain better insights into the spin pumping mechanisms.

Experimental observation of a clear exponential decay of dynamic spin pumping provides decisive evidence for, and quantitative understanding of a fundamental spin pumping mechanism. This result points to the important ability to tune characteristics of spin functional devices and reveal new phenomena.

Acknowledgements

This work is supported by the Center for Emergent Materials at the Ohio State University, a NSF Materials Research Science and Engineering Center (DMR-0820414) (HLW, YP, and FYY) and by the Department of Energy through grant DE-FG02-03ER46054 (PCH). Partial support is provided by Lake Shore Cryogenics Inc. (CHD) and the NanoSystems Laboratory at the Ohio State University.

Reference:

1. Žutić, I., Fabian, J. & Das Sarma, S. Spintronics: Fundamentals and applications. *Rev. Mod. Phys.* **76**, 323 (2004).
2. Tserkovnyak, Y., Brataas, A. & Bauer, G. E. W. Enhanced Gilbert damping in thin ferromagnetic Films. *Phys. Rev. Lett.* **88**, 117601 (2002).
3. Kovalev, A. A., Brataas, A., & Bauer, G. E. W. Spin transfer in diffusive ferromagnet–normal metal systems with spin-flip scattering. *Phys. Rev. B* **66**, 224424 (2002).
4. Tserkovnyak, Y., Brataas, A. & Bauer, G. E. W. Spin pumping and magnetization dynamics in metallic multilayers. *Phys. Rev. B* **66**, 224403 (2002).
5. Tserkovnyak, Y., Brataas, A. & Bauer, G. E. W. & Halperin, B. I. Nonlocal magnetization dynamics in ferromagnetic heterostructures. *Rev. Mod. Phys.* **77**, 1375 (2005).
6. Kajiwara, Y. *et al.* Transmission of electrical signals by spin-wave interconversion in a magnetic insulator. *Nature* **464**, 262 (2010).
7. Parkin, S. S. P. Origin of enhanced magnetoresistance of magnetic multilayers: Spin dependent scattering from magnetic interface states. *Phys. Rev. Lett.* **71**, 1641 (1993).
8. Mosendz, O., Pearson, J. E., Fradin, F.Y., Bader, S. D., and Hoffmann, A. Suppression of spin-pumping by a MgO tunnel-barrier. *Appl. Phys. Lett.* **96**, 022502 (2010).
9. Hauser, A. J. *et al.* Unlocking the potential of half-metallic Sr₂FeMoO₆ films through controlled stoichiometry and double-perovskite ordering. *Phys. Rev. B* **83**, 014407 (2011).
10. Hauser, A. J. *et al.* Fully ordered Sr₂CrReO₆ epitaxial films: A high-temperature ferrimagnetic semiconductor. *Phys. Rev. B* **85**, 161201(R) (2012).
11. C. H. Du, *et al.* Control of Magnetocrystalline Anisotropy by Epitaxial Strain in Double Perovskite Sr₂FeMoO₆ Films. *Phys. Rev. Lett.* **110**, 147204 (2013).

12. Hauser, A. J. *et al.* Electronic and magnetic tunability of Sr₂CrReO₆ films by growth-mediated oxygen modulation. *Appl. Phys. Lett.* **102**, 032403 (2013).
13. Farley, M. Ferromagnetic resonance of ultrathin metallic layers. *Rep. Prog. Phys.* **61**, 755 (1998).
14. Heinrich, B. *et al.* Spin pumping at the magnetic insulator (YIG)/normal metal (Au) interfaces. *Phys. Rev. Lett.* **107**, 066604 (2011).
15. Saitoh, E., Ueda, M., Miyajima, H. & Tatara, G. Conversion of spin current into charge current at room temperature: Inverse spin-Hall effect. *Appl. Phys. Lett.* **88**, 182509 (2006).
16. Valenzuela, S. O. & Tinkham, M. Direct electronic measurement of the spin Hall effect. *Nature* **442**, 176 (2006).
17. Ando, K. *et al.* Electrically tunable spin injector free from the impedance mismatch problem. *Nature Materials* **10**, 655 (2011).
18. Ando, K. *et al.* Inverse spin-Hall effect induced by spin pumping in metallic system. *J. Appl. Phys.* **109**, 103913 (2011).
19. Harder, M. *et al.* Analysis of the line shape of electrically detected ferromagnetic resonance. *Phys. Rev. B* **84**, 054423 (2011).
20. Huang, S. Y. *et al.* Transport magnetic proximity effects in Platinum. *Phys. Rev. Lett.* **109**, 107204 (2012).
21. Costache, M. V. *et al.* Electrical detection of spin pumping due to the precessing magnetization of a single ferromagnet. *Phys. Rev. Lett.* **97**, 216603 (2006).
22. Shimizu, T., and Okushi, H., Intrinsic electrical properties of Au/SrTiO₃ Schottky junctions. *J. Appl. Phys.* **85**, 7244 (1999).

23. Lide, D. R., *Handbook of Chemistry and Physics* (CRC Press, Taylor & Francis Group, New York, 86th Edition, 2005).
24. Shankar, R., *Principles of Quantum Mechanics* (Springer, New York, 2nd Edition, 1994).
25. E.Shikoh *et al.*, Spin-pump-induced spin transport in *p*-Type Si at room temperature. *Phys. Rev. Lett.* **110**, 127201 (2013).

Figure Captions:

Figure 1. **a** Semi-log θ - 2θ XRD scan of a 20-nm thick YIG film on GGG(111), which exhibits clear Laue oscillations corresponding to the film thickness. Inset: rocking curve of the YIG (444) peak. **b** Representative room-temperature FMR derivative spectrum of a 20-nm YIG film with \mathbf{H} in plane at $P_{\text{rf}} = 0.2$ mW, which gives a peak-to-peak linewidth of 10 Oe. **c** Schematics of experimental setup for ISHE voltage measurements for Pt/YIG and Pt/barrier/YIG samples. **d** V_{ISHE} vs. H spectra and **e** FMR derivative spectrum of a Pt(5nm)/YIG(20nm) bilayer at $P_{\text{rf}} = 200$ mW. **f** Angular dependence of normalized V_{ISHE} of the Pt/YIG bilayer (the green curve is a simple calculation of $\sin\theta_{\text{H}}$). **g** rf power dependence of V_{ISHE} with a least-squares fit.

Figure 2. V_{ISHE} vs. H spectra of Pt/barrier/YIG multilayers with 0.5-nm thick **a** $\text{Sr}_2\text{GaTaO}_6$, **b** $\text{Sr}_2\text{CrNbO}_6$, and **c** Si barriers at $P_{\text{rf}} = 200$ mW, with the corresponding FMR derivative spectra shown in **d**, **e**, **f**, respectively. Angular dependencies of the normalized V_{ISHE} in **g**, **h**, **i** follow $\sin\theta_{\text{H}}$ (green curves), and the rf power dependencies of V_{ISHE} in **j**, **k**, **l** show linear behavior for all three samples.

Figure 3. Semi-log plots of V_{ISHE} normalized to the values for Pt/YIG bilayers with direct contact as a function of the barrier thickness of **a** Pt/ $\text{Sr}_2\text{GaTaO}_6$ /YIG, **b** Pt/ $\text{Sr}_2\text{CrNbO}_6$ /YIG, and **c** Pt/Si/YIG, with four representative V_{ISHE} vs. H spectra of various barrier thicknesses for each series shown in **d**, **e**, and **f**, respectively. The solid lines in **a**, **b**, and **c** are least-squares fits, which indicate exponential decay of ISHE voltages with decay length $\lambda = 0.16, 0.23,$ and 0.74 nm for Pt/ $\text{Sr}_2\text{GaTaO}_6$ /YIG, Pt/ $\text{Sr}_2\text{CrNbO}_6$ /YIG, and Pt/Si/YIG, respectively.

Figure 4. Schematics of band structures of **a** Pt/ $\text{Sr}_2\text{GaTaO}_6$ /YIG and **b** Pt/ $\text{Sr}_2\text{CrNbO}_6$ /YIG heterostructures with an estimated Schottky barrier height Φ_{B} at half of the bandgap for each material. The blue curves in **a** and **b** illustrate the quantum tunneling of the electron

wavefunction from Pt into the barrier. **c** Inverse of decay length, $1/\lambda$, as a function of $\sqrt{\Phi_B}$ for Pt/Sr₂GaTaO₆/YIG and Pt/Sr₂CrNbO₆/YIG. The solid markers are experimental data and the solid line connecting the two points and origin is guide to the eye.

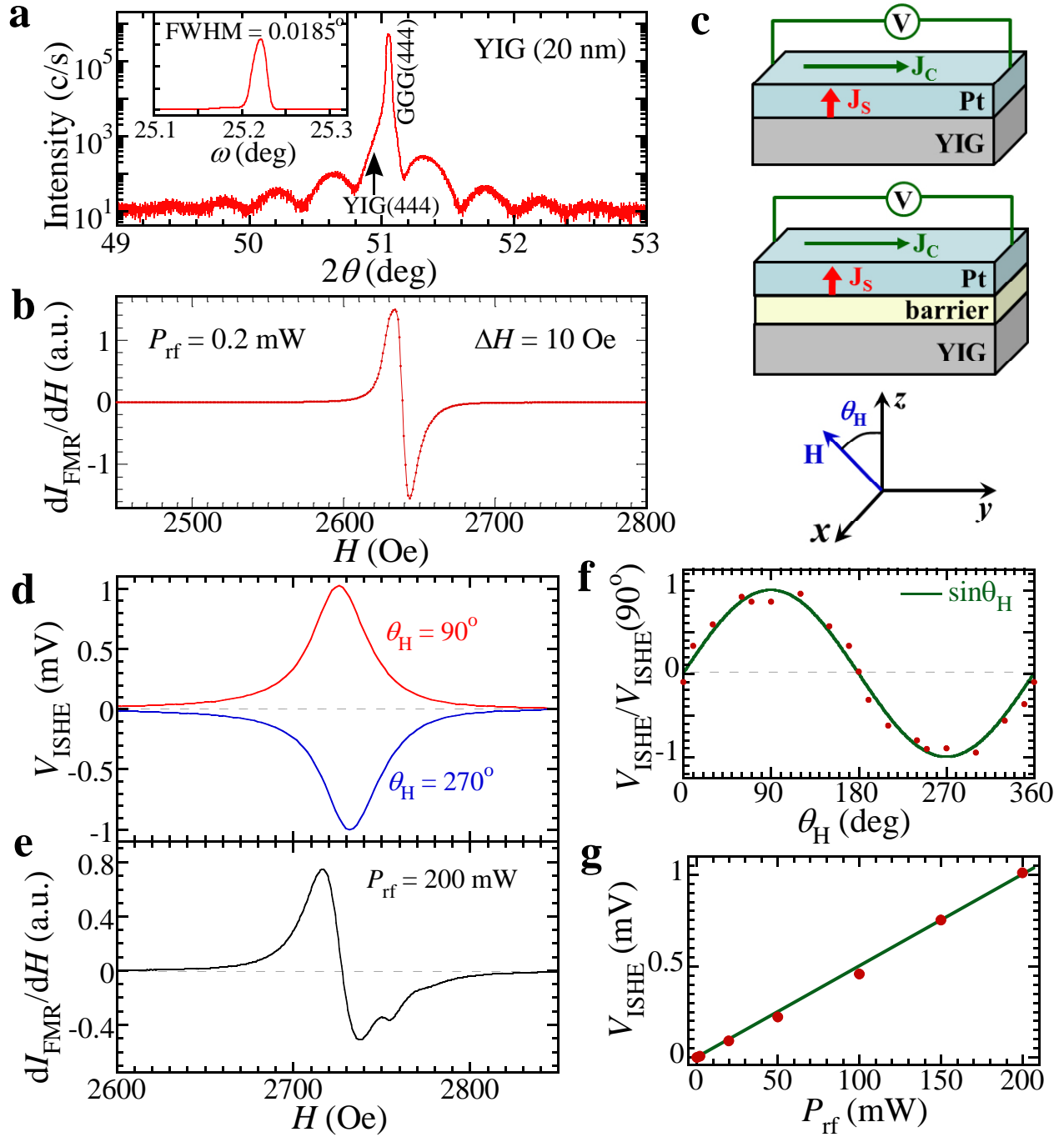


Fig. 1.

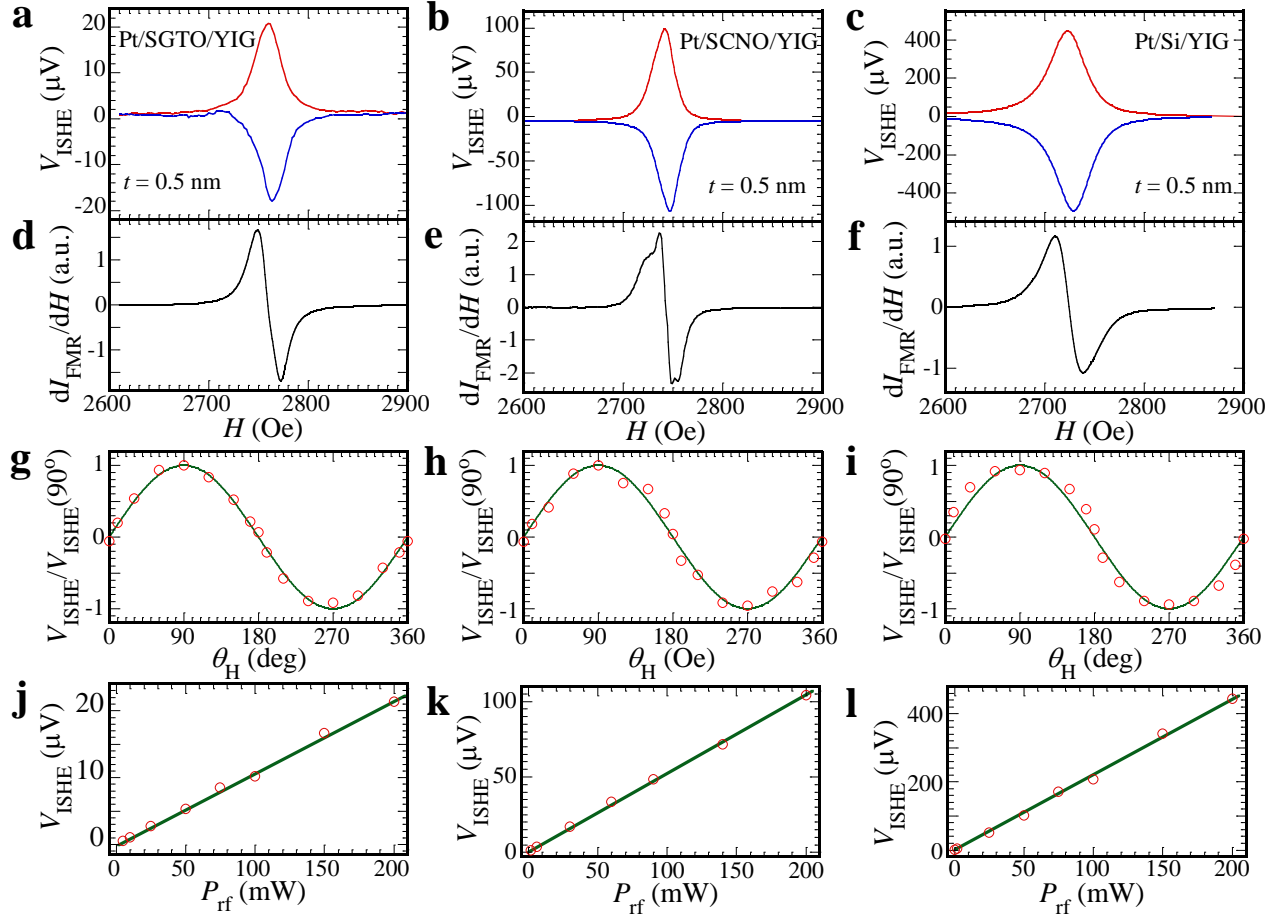


Fig. 2.

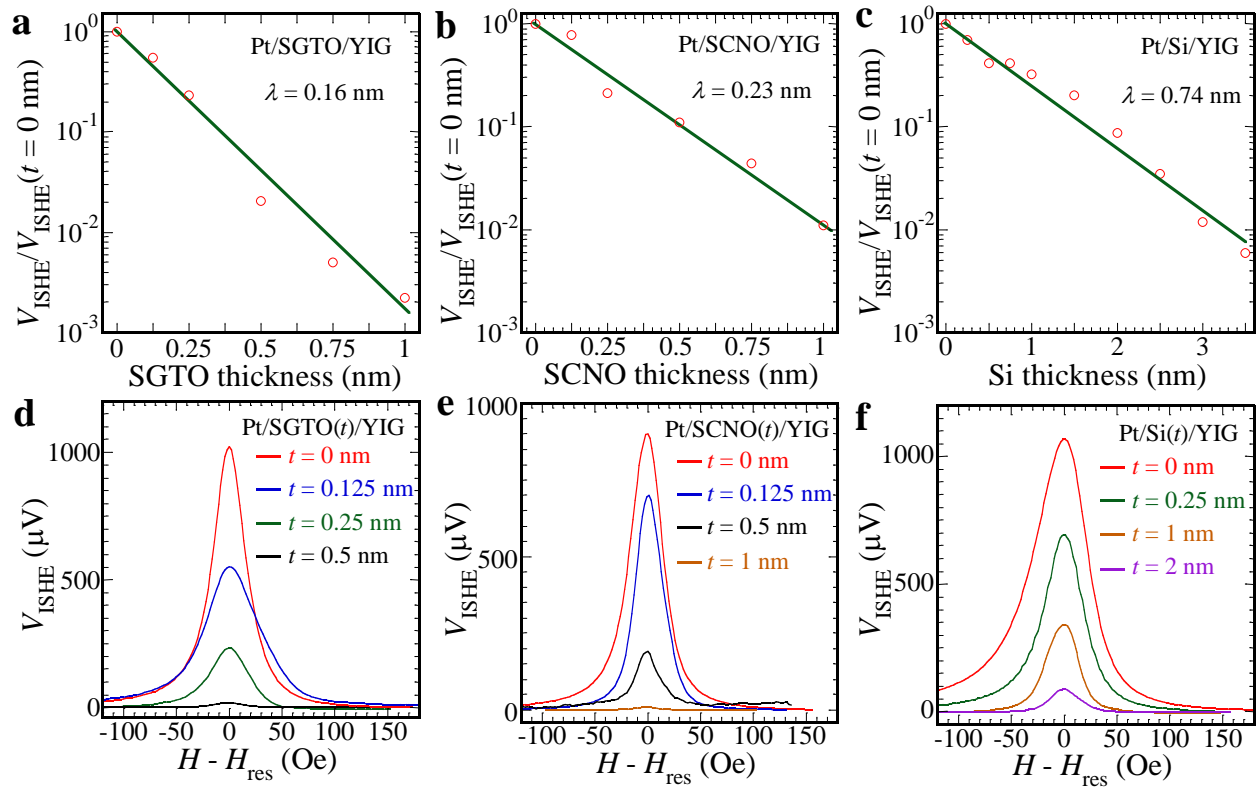


Fig. 3.

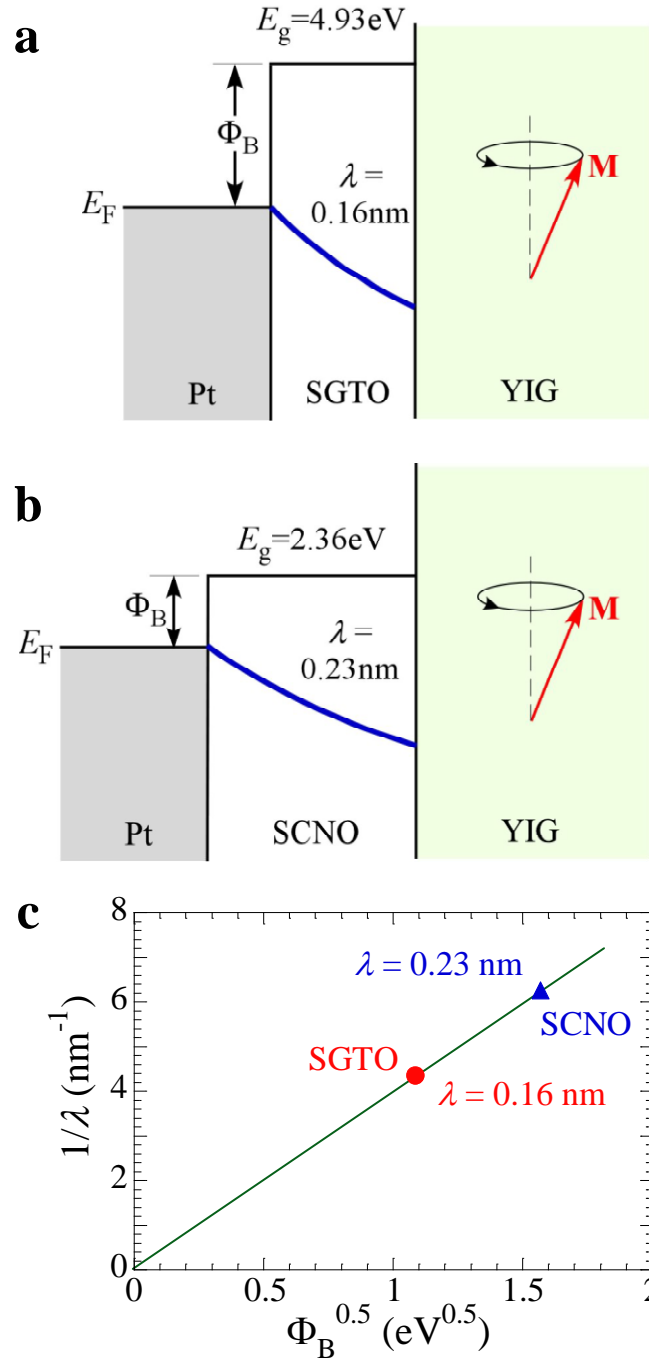


Fig. 4.

Supplementary Information

1. Growth of $\text{Y}_3\text{Fe}_5\text{O}_{12}$, Pt and Si layers

Single-crystalline $\text{Y}_3\text{Fe}_5\text{O}_{12}$ (YIG) epitaxial thin films were grown on (111)-oriented $\text{Gd}_3\text{Ga}_5\text{O}_{12}$ (GGG) substrates in an off-axis ultrahigh vacuum (UHV) sputtering system [S1-S3] with a base pressure below 5×10^{-9} Torr. The optimal growth conditions include: a total Ar/ O_2 pressure of 11.5 mTorr with an O_2 concentration of 0.15%, a substrate temperature 750 °C, and a radio-frequency (rf) sputtering power of 50 W. The deposition rate of YIG films is 0.33 nm/min. Crystal structure of the films was characterized by a Bruker D8 high resolution x-ray diffraction (XRD) system. Polycrystalline Pt and amorphous Si layers were deposited in the same sputtering system in pure Ar at room temperature using off-axis geometry. The deposition rates of Pt and Si are between 1 and 1.6 nm/min. Both in-situ and ex-situ growths of the Pt layers were carried out to test whether exposing the YIG films to air would affect the Pt/YIG interface quality and the efficiency of spin pumping. However, no difference in the magnitude of the spin pumping signals is observed between the two growth modes.

2. $\text{Sr}_2\text{GaTaO}_6$ and $\text{Sr}_2\text{CrNbO}_6$ barriers

$\text{Sr}_2\text{GaTaO}_6$ (SGTO) and $\text{Sr}_2\text{CrNbO}_6$ (SCNO) are both insulators with the $A_2BB'O_6$ double perovskite structure, which can be viewed as combination of two different single perovskites (similar to SiTiO_3). Double perovskites exhibit a broad range of interesting properties due to their complexity and tenability, and have been used in various applications. For example, LSAT is a commonly used single crystal substrate for epitaxial film growth with the composition

(LaAlO₃)_{0.3}(Sr₂AlTaO₆)_{0.7} [S4], of which the majority phase (Sr₂AlTaO₆) is a double perovskite very similar to the Sr₂GaTaO₆ used in this report. Sr₂CrNbO₆ has an almost identical lattice constant as Sr₂GaTaO₆ ($a = 0.788$ nm) and have been used as an epitaxial buffer layer for subsequent growth of other double perovskite epitaxial films [S5].

Thin Sr₂GaTaO₆ and Sr₂CrNbO₆ layers of various thicknesses were deposited on YIG films in the same sputtering system at room temperature by rf sputtering using a power of 50 W. The Ar/O₂ sputtering pressure is 12.5 mTorr and the O₂ concentration is between 0.15% and 0.20%. The deposition rates are 2.2 and 0.50 nm/min for Sr₂CrNbO₆ and Sr₂GaTaO₆, respectively.

3. Characterization of band gap by UV-visible absorption

Diffuse reflectance (R) spectra of the Sr₂CrNbO₆ and Sr₂GaTaO₆ samples were collected on an Ocean Optics USB4000-UV-VIS miniature fiber optic spectrometer using a Spectralon® standard. The percent reflectance was transformed using the Kubelka-Munk function [S6, S7], $F(R) = \frac{(1-R)^2}{2R}$, and is shown in Fig. S1. The intersection of the linear fit and photon energy axis gives band gaps of 4.93 eV (Sr₂GaTaO₆) and 2.36 eV (Sr₂CrNbO₆).

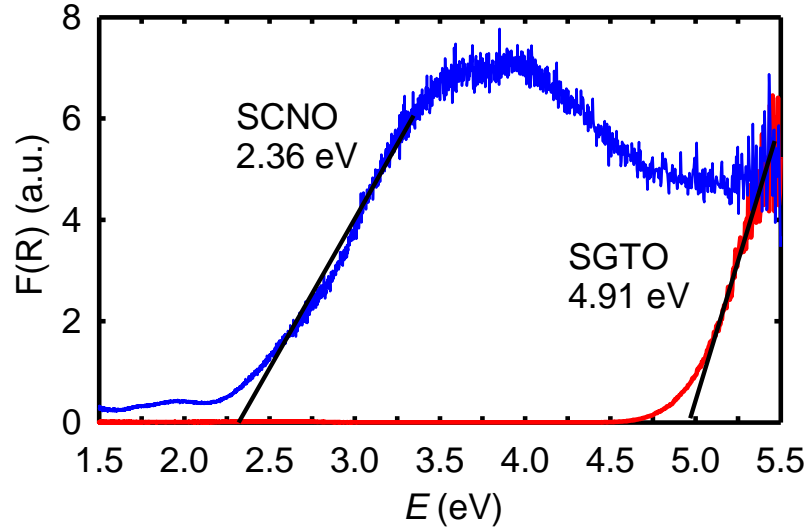


Figure S1: UV-visible absorption spectra for $\text{Sr}_2\text{GaTaO}_6$ (red) and $\text{Sr}_2\text{CrNbO}_6$ (blue) using the Kubelka-Munk function, $F(R) = \frac{(1-R)^2}{2R}$, where R is the reflectance. From the intersection of the absorption edges and the x-axis, the band gaps of 4.93 and 2.36 eV are obtained for $\text{Sr}_2\text{GaTaO}_6$ and $\text{Sr}_2\text{CrNbO}_6$, respectively.

Reference:

- S1. A. J. Hauser *et al.*, *Phys. Rev. B* **83**, 014407 (2011).
- S2. A. J. Hauser *et al.*, *Phys. Rev. B: Rapid Communications* **85**, 161201(R) (2012).
- S3. C. H. Du, *et al.*, *Phys. Rev. Lett.* **110**, 147204 (2013).
- S4. <http://mtixtl.com/lstat.aspx>.
- S5. A. J. Hauser *et al.* *Appl. Phys. Lett.* **102**, 032403 (2013).
- S6. P. Kubelka and F. Z. Munk, *Technol. Phys.* **12**, 593 (1931).
- S7. P. Kubelka, *J. Opt. Soc. Am.* **38**, 448 (1947).